

**Titre:** Design and experimental validation of a new outer rotor double PM excited flux switching generator for direct drive wind turbines

**Auteurs:** Mohammad Farahzadi, Saima Ali, Seyedarmin Mirnikjoo, Karim Abbaszadeh, Fabrizio Marignetti, & Maryam Salehi

**Date:** 2024

**Type:** Article de revue / Article

**Référence:** Farahzadi, M., Ali, S., Mirnikjoo, S., Abbaszadeh, K., Marignetti, F., & Salehi, M. (2024). Design and experimental validation of a new outer rotor double PM excited flux switching generator for direct drive wind turbines. IEEE Access, 12, 62256-62267. <https://doi.org/10.1109/access.2024.3394968>

## Document en libre accès dans PolyPublie

Open Access document in PolyPublie

**URL de PolyPublie:** <https://publications.polymtl.ca/58559/>

PolyPublie URL:

**Version:** Version officielle de l'éditeur / Published version  
Révisé par les pairs / Refereed

**Conditions d'utilisation:** Creative Commons Attribution 4.0 International (CC BY)

Terms of Use:

## Document publié chez l'éditeur officiel

Document issued by the official publisher

**Titre de la revue:** IEEE Access (vol. 12)

Journal Title:

**Maison d'édition:** IEEE

Publisher:

**URL officiel:** <https://doi.org/10.1109/access.2024.3394968>

Official URL:

**Mention légale:**

Legal notice:



Received 7 April 2024, accepted 21 April 2024, date of publication 30 April 2024, date of current version 8 May 2024.

Digital Object Identifier 10.1109/ACCESS.2024.3394968

## RESEARCH ARTICLE

# Design and Experimental Validation of a New Outer Rotor Double PM Excited Flux Switching Generator for Direct Drive Wind Turbines

MOHAMMAD FARAHZADI<sup>1</sup>, SALMAN ALI<sup>2</sup>, (Graduate Student Member, IEEE),  
SEYEDARMIN MIRNIKJOO<sup>3</sup>, KARIM ABBASZADEH<sup>4</sup>, (Senior Member, IEEE),  
FABRIZIO MARIGNETTI<sup>2</sup>, (Senior Member, IEEE), AND MARYAM SALEHI<sup>5</sup>

<sup>1</sup>Faculty of Electrical Engineering, University of Science and Culture, Tehran 1461968151, Iran

<sup>2</sup>Department of Electrical and Information Engineering (DIEI), University of Cassino and Southern Lazio, 03043 Cassino, Italy

<sup>3</sup>Electrical Engineering Department, Polytechnique Montréal, Montreal, QC H3C 3A7, Canada

<sup>4</sup>Faculty of Electrical Engineering, K. N. Toosi University of Technology, Tehran 15433-19967, Iran

<sup>5</sup>Department of Electrical and Computer Engineering, The University of North Carolina at Charlotte, Charlotte, NC 28223, USA

Corresponding author: Salman Ali (salman.ali@unicas.it)

This work was supported by the MOST Sustainable Mobility Center through European Union Next-Generation EU (PIANO NAZIONALE DI RIPRESA E RESILIENZA (PNRR)—MISSIONE 4 COMPONENTE 2, INVESTIMENTO 1.4—D.D. 1033), in June 2022, under Grant CN00000023.

**ABSTRACT** An outer rotor double permanent magnet (PM) excited flux switching generator is designed and optimized in this paper for direct drive wind turbine applications. This generator consists of two sets of PMs: ferrite PMs embedded in the stator yoke and neodymium PMs sandwiched between the rotor segments. In this regard, the main justification for employing ferrite PMs in the stator yoke is that the risk of demagnetization of ferrite PMs at high temperatures is lower than that of neodymium PMs (the temperature of the machine's stationary parts is higher than that of its rotating parts). For the design of the machine, the Taguchi design of experiments is deployed, while a decision-making algorithm based on the technique for order of preference by similarity to the ideal solution is used to solve the contradiction that results from the Taguchi design of experiments in the multi-objective design optimization process. During the multi-objective design optimization steps, simultaneously maximizing the no-load phase voltage and minimizing the cogging torque and total harmonic distortion of the no-load phase voltage are defined as the objective functions. The optimally designed machine is prototyped and subsequently subjected to experimental validation to verify the predictions in satisfying the objective functions.

**INDEX TERMS** DMA-TOPSIS, DPME-FSG, ETD, multi-objective optimization, POCs, wind turbine.

## NOMENCLATURE

FSPM	Flux Switching Permanent Magnet.
DDWT	Direct Drive Wind Turbine.
PM	Permanent Magnet.
DPME-FSG	Double Permanent Magnet Excited Flux Switching Generator.

THD	Total Harmonic Distortion.
ETD	Taguchi Design of Experiments.
POCs	Possible Optimum Combinations.
DMA-TOPSIS	Decision-Making Algorithm based on the Technique for Order of Preference by Similarity to the Ideal Solution.
MEC	Magnetic Equivalent Circuit.
MMF	Magneto-Motive Force.
HAWT	Horizontal Axes Wind Turbine.
VAWT	Vertical Axes Wind Turbine.

The associate editor coordinating the review of this manuscript and approving it for publication was Xiaodong Liang<sup>id</sup>.



DVs	Design Variables.
OFs	Objective Functions.
MA	Analysis of Mean.
DM	Decision Matrix.
WD	Weighted Decision.
SD	Separation Distance.
PIS	Positive Ideal Solution.
NIS	Negative Ideal Solution.
$C_i$	Relative closeness of each possible optimum combination to the ideal solution.
3-D FEM	three-dimensional Finite Element Method.

## I. INTRODUCTION

Wind power generation systems are one of the most attractive renewable energy sources from scientific and industrial viewpoints due to their high reliability, affordable costs, and lack of harmful effects on the environment [1], [2], [3]. Since the elimination of gearboxes can result in more efficient wind power generation systems, generators with an inherent magnetic-gearing effect have attracted attention [4], [5]. FSPM generators are one of the modern synchronous generators that are employed in DDWT applications, and the rotor structure of FSPM machines is often identical to that of switched reluctance machines, without any windings or PMs [6], [7]. In the conventional topologies of FSPM machines, both the armature windings and the excitation system are located on the stator structure, and significant amounts of PMs are usually used in their structure [8], [9]. In [10] and [11], two separate outer rotor FSPM machines were introduced. In [10], the rotor core was segmented, and the neodymium PMs were mounted on the stator teeth. In [11], the neodymium PMs were sandwiched on the stator teeth. In contrast, two different inner rotor FSPM machines were presented in [12] and [13]. In [12], the stator core was divided into segments, and the neodymium PMs were positioned inside the stator teeth; in [13], the neodymium PMs were situated between the stator teeth. Furthermore, the inner rotor FSPM machine was discussed in [14] and [15], incorporating neodymium PMs placed in both the radial and circumferential directions within the stator core. In this regard, one of the challenges that may be encountered with conventional FSPM machines, such as the outer rotor FSPM machines that have been discussed in [10] and [11], or such as the inner rotor FSPM machines that have been reported in [12] to [15], is the demagnetization of PMs. This is because the PMs are located in the stator core, which has a higher temperature compared to the rotor core. Also, the neodymium PMs lose their magnetization properties when they are exposed to high temperatures. Therefore, in order to avoid the demagnetization of PMs, the neodymium PMs of the proposed outer rotor generator are sandwiched between the rotor segments, which have a much lower temperature compared to the stationary parts. In addition, the ferrite PMs,

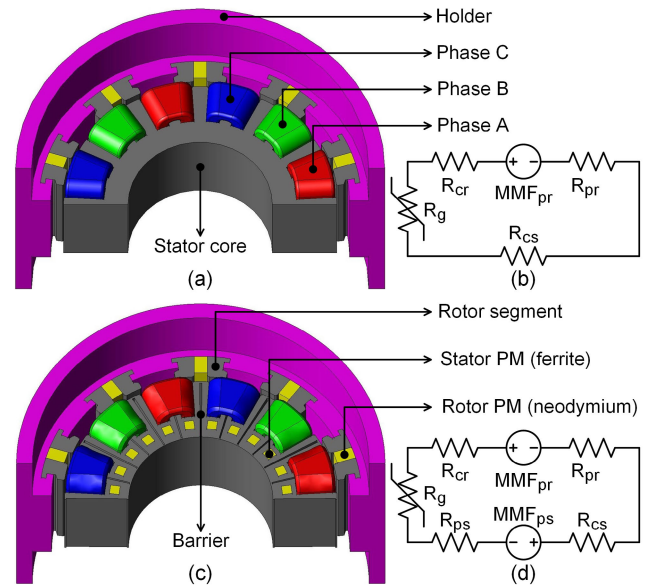


**FIGURE 1.** (a) 3-D view of the basic topology; (b) MEC of the basic topology; (c) 3-D view of the DPME-FSG; and (d) MEC of the DPME-FSG.

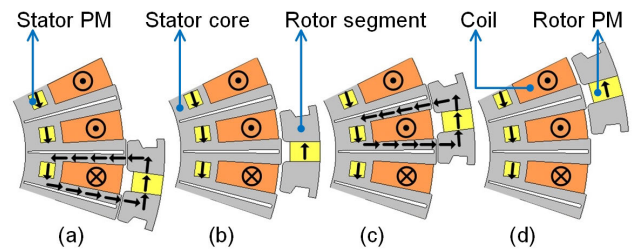


**FIGURE 2.** (a) Rotor at the first position, (b) rotor at the second position, (c) rotor at the third position, and (d) rotor at the fourth position.

which are strong at high temperatures, are located in the stator yoke [16], [17].

The proposed generator, known as the double permanent magnet excited flux switching generator (DPME-FSG), incorporates both ferrite and neodymium PMs in the stator yoke and rotor segments, respectively. Compared to conventional FSPM machines, this design provides higher power density and a lower volume of neodymium PMs, which are more costly than ferrite PMs. Furthermore, in order to improve the no-load phase voltage, cogging torque, and THD% of the no-load phase voltage in the initial design of the DPME-FSG, the multi-objective design optimization is conducted in three steps: ETD, POCs, and DMA-TOPSIS.

This paper is organized as follows: Section II discusses the structure and concept of the DPME-FSG, while Section III covers its design procedure. Section IV details the multi-objective optimization steps of the DPME-FSG, whereas Section V evaluates its performance. In Section VI, the results of the prototyped DPME-FSG's optimization targets are laboratory verified.



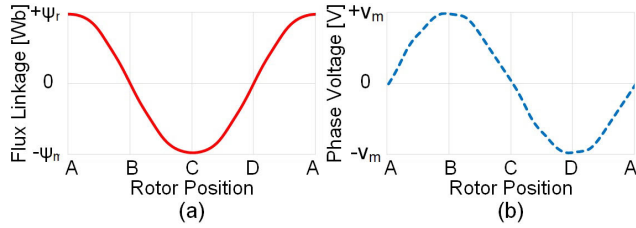


**FIGURE 3.** (a) Flux linkage among an electric cycle and (b) induced voltage among an electric cycle.

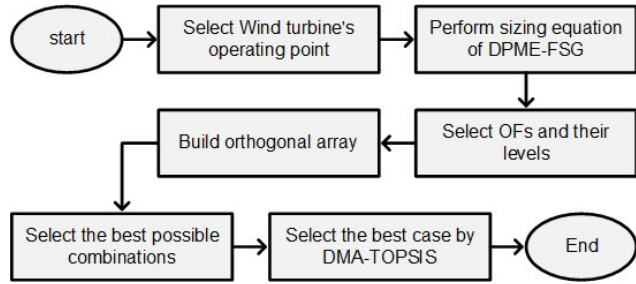


**FIGURE 4.** Flowchart of the design and optimization of the DPME-FSG.

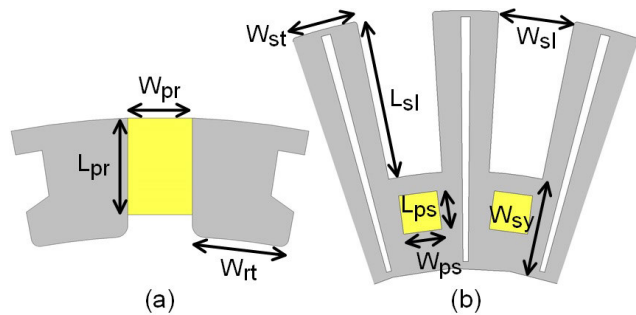


**FIGURE 5.** The defined dimensions of the DPME-FSG in (a) Rotor segment and (b) stator core.

## II. CONCEPT OF DPME-FSG

Figure 1 shows the structure and MEC related to DPME-FSG and its basic topology. As shown in this figure, the ferrite PMs in the stator yoke and the barriers in the stator teeth distinguish the DPME-FSG from the basic topology. The DPME-FSG incorporates two various types of PMs, one in the rotor and one in the stator. In this regard, the magnetization direction of the rotor PMs (neodymium), which are sandwiched between the rotor segments, is counter-clockwise, but that of the stator PMs (ferrite), which are located inside the stator yoke, is clockwise. Additionally, the magnetization directions of the rotor PM and stator PM have been selected in such a way that the resultant MMF at a pole of the DPME-FSG is boosted. Also, two benefits result from incorporating ferrite PMs into the stator yoke of the DPME-FSG. Firstly, ferrite PMs do not experience demagnetization because the temperature of the machine's stationary parts is higher than that of its rotating parts, and the demagnetization risk related to ferrite PM at high temperatures is lower than that of neodymium PM. Secondly, ferrite PMs are

significantly more affordable compared to neodymium PMs. Moreover, the flux barriers are provided in the stator teeth of the DPME-FSG to separate the positive and negative half cycles of flux linkage between the rotor segments and stator teeth. As a consequence, the power density of the DPME-FSG is higher than that of the basic topology, and in addition to the increased power density, the smaller volume of PMs and greater resistance of PMs against demagnetization are other benefits of the DPME-FSG over conventional FSPM machines. According to the MECs shown in Fig. 1,  $MMF_{pr}$  and  $MMF_{ps}$  relate to the MMF source that is led by the rotor PMs and the stator PMs, respectively. In this context, the leakage reluctance of rotor PMs and stator PMs is referred to as  $R_{pr}$  and  $R_{ps}$ , respectively. Additionally, the reluctance of the rotor segments and the stator core, which are respectively known as  $R_{cr}$  and  $R_{cs}$ , are both constant. On the other hand, the salient pole structure of FSPM machines causes the air-gap reluctance ( $R_g$ ) to be variable during an electric cycle. The flux linkage path in four different rotor positions during an electric cycle is shown in Fig. 2. As shown in Fig. 2 (a), the air-gap reluctance is at its minimum due to the alignment of the rotor segments and stator teeth, which causes the flux linkage to reach its maximum value. When the rotor PM is aligned with the stator tooth (see Fig. 2(b)) and flux leakage is ignored, the flux linkage is zero because the air-gap reluctance is at its maximum value. Fig. 2 (c) demonstrates that in the third position during an electric cycle, the rotor segments and stator teeth will be aligned, and the air-gap reluctance will be at its lowest value, identical to the first position depicted in Fig. 2 (a). The values of flux linkage in the first and third positions are the same; however, the signs are different due to the fact that the flux linkage paths in the first and third positions are located among the inward and outward sides of the coil, respectively. The flux linkage in the fourth position during an electric cycle (see Fig. 2 (d)) is similar to the second position (see Fig. 2 (b)). On top of that, Fig. 3 (a) shows the flux linkage during an electric cycle, while Fig. 3 (b) depicts the induced voltage during an electric cycle, which is the derivation of the flux linkage during an electric cycle. It can be seen that the rotation of the salient pole rotor of the DPME-FSG leads to the induction of a sinusoidal voltage during an electric cycle in a phase coil.

## III. DESIGN OF DPME-FSG

The design procedures of the DPME-FSG, which has been developed for use in DDWT, are going to be discussed in this section. In this regard, the design and multi-objective optimization processes of the DPME-FSG are depicted in Fig. 4. This flowchart shows that selecting the operating point of the wind turbine is the first step in the design process.

### A. WIND TURBINE SPECIFICATION

The HAWT and VAWT are two common wind turbine types. This paper employs HAWT instead of VAWT due to the higher wind energy absorption and efficacy of HAWT.



**TABLE 1.** Initial design parameters of DPME-FSG.

Parameter	Value	Unit
Stator slot number	24	-
Rotor pole number	10	-
Air-gap length	0.65	mm
Turns per coil	200	-
Stator height	60	mm
Rotor height	70	mm
Rotor outer diameter	200.7	mm
Shaft diameter	90	mm
Rotational speed	750	rpm
Frequency	125	Hz
Residual flux density of rotor PM	1.2	T
Residual flux density of stator PM	0.41	T
Neodymium PMs cost	~41.5	\$
Ferrite PMs cost	~1.5	\$
Phase current	3.1	A
Efficiency	86.93	%
Nominal power	2300	W

Furthermore, (1) provides the DDWT power [18].

$$P_T = 0.5C_P A_W V^3 \quad (1)$$

where,  $P_T$  is HAWT's power [W],  $C_P$  is power coefficient of HAWT,  $A_W$  is blades swept area [ $\text{m}^2$ ], and  $V$  is wind velocity [m/s]. In this context, the tip-speed ratio and blade pitch angle determine the power coefficient of the turbine. Furthermore, the tip-speed ratio ( $\lambda$ ) is expressed by (2), where  $\omega_r$  is the turbine's angular velocity and  $R$  is the blade radius.

$$\lambda = \frac{\omega_r R}{V} \quad (2)$$

Moreover, the equation presented in (3), which depicts the relation between the turbine's nominal power and rated speed, is one of the most determining factors of the machine's design procedure.

$$\omega_r \propto P_T^{-0.487} \quad (3)$$

## B. INITIAL DESIGN

The performance of DPME-FSG is highly dependent on the number of rotor poles, as the rotor poles are responsible for flux modulation in the DPME-FSG. In this regard, (4) and (5) present the equation of the machine's synchronous frequency and the relation between the number of rotor poles and the number of stator slots, where  $f_s$ ,  $n_m$ ,  $N_r$ , and  $N_s$  are the synchronous frequency, the synchronous speed, the number of rotor poles, and the number of stator slots, respectively [19].

$$f_s = \frac{n_m N_r}{60} \quad (4)$$

$$N_s = 2(N_r \pm a), a = 1, 2, 3, \dots \quad (5)$$

**TABLE 2.** DVs of DPME-FSG.

DVs	Definition	Symbol	Unit
DV1	Width of the rotor PM	$W_{pr}$	mm
DV2	Width of the stator PM	$W_{ps}$	mm
DV3	Rotor tooth angle	$W_{rt}$	deg
DV4	Stator tooth angle	$W_{st}$	deg

**TABLE 3.** Levels of DVs.

DVs	Level 1	Level 2	Level 3	Level 4	Level 5
DV1	6	6.5	7	7.5	8
DV2	4.5	5	5.5	6	6.5
DV3	6.5	7.5	8.5	9.5	10.5
DV4	7	7.5	8	8.5	9

The equation for the outer diameter of the stator ( $D_{so}$ ) is given in (6), where  $T_e$  is the electromagnetic torque generated by the interaction of magnetic loading and electric loading,  $B_v$  is the magnetic loading,  $A_{\omega v}$  is the armature winding electrical loading of the harmonic with  $v$ -pole-pair,  $\cos \varphi_v$  is the load power factor, and  $l_a$  is the active length of the machine [20].

$$D_{so} = \sqrt{\frac{T_e}{\frac{\pi}{4} B_v A_{\omega v} \cos \varphi_v l_a}} \quad (6)$$

The armature winding electrical loading of the harmonic with  $v$ -pole-pair is expressed in (7), in which  $m$  is the phase number,  $N_{ph}$  is the phase turn number,  $k_{\omega v}$  is the winding factor of  $v$ th order, and  $I_{\max}$  is the maximum armature current value.

$$A_{\omega v} = \frac{m N_{ph} k_{\omega v} I_{\max}}{\pi D_{so}} \quad (7)$$

In addition, the rotor pole arc coefficient ( $C_s$ ) can be applied to determine the rotor tooth angle (see Fig. 5) using (8) and (9), where,  $W_{rt}$  and  $B_{avg}$  are the rotor tooth angle and the average magnetic flux density, respectively.

$$W_{rt} \approx \frac{\pi C_s}{N_r} \quad (8)$$

$$C_s = \frac{B_{avg}}{B_v} \quad (9)$$

Moreover, the dimensions of PMs in the rotor segments and stator yoke can be determined using equations (10) to (15) (see Figs. 1 and 5):

$$MMF = (R_{cr} + R_{cs} + R_g + R_{pr} + R_{ps})\varphi \quad (10)$$

$$MMF = MMF_{pr} + MMF_{ps} \quad (11)$$

$$MMF_{pr} = B_{pr} L_{pr} H_{pr} \quad (12)$$

$$R_{pr} = \frac{W_{pr}}{\mu_0 \mu_r L_{pr} H_{pr}} \quad (13)$$

$$MMF_{ps} = B_{ps} L_{ps} H_{ps} \quad (14)$$



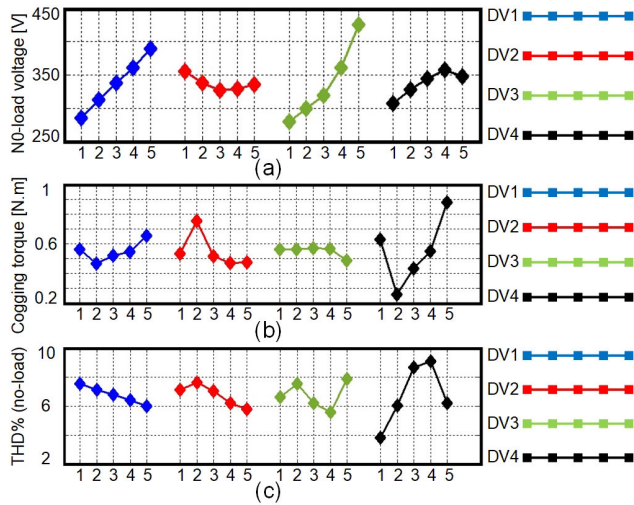


FIGURE 6. MA of (a) no-load voltage, (b) cogging torque, and (c) THD% (for no-load phase voltage).

$$R_{ps} = \frac{W_{ps}}{\mu_0 \mu_r L_{ps} H_{ps}} \quad (15)$$

Here,  $\varphi$  represents the flux between the stator teeth and the rotor segments,  $B_{pr}$  is the residual flux density of the rotor PM,  $L_{pr}$  is the length of the rotor PM,  $H_{pr}$  is the height of the rotor segments,  $W_{pr}$  is the width of the rotor PM,  $\mu_0$  is the air permeability, and  $\mu_r$  is the relative permeability. Also,  $B_{ps}$  is the residual flux density of the stator PM,  $L_{ps}$  is the length of the stator PM,  $H_{ps}$  is the height of the stator core, and  $W_{ps}$  is the width of the stator PM (see Figs. 1 and 5). The dimensions of the stator core can also be obtained using the following relations (see Fig. 5):

$$D_{so} - D_{sh} = 2(W_{sy} + L_{sl}) \quad (16)$$

$$L_{sl} = \frac{A_c}{k_f W_{sl}} \quad (17)$$

$$\tau_s = W_{sl} + W_{st} \quad (18)$$

where  $D_{sh}$  is the diameter of the shaft,  $W_{sy}$  is the width of the stator yoke,  $L_{sl}$  is the length of the stator slot,  $A_c$  is the coil side surface,  $k_f$  is the fill factor,  $W_{sl}$  is the slot width of the stator,  $\tau_s$  is the pole pitch of the stator, and  $W_{st}$  is the width of the stator tooth. In this regard, Table 1 presents the specifications of DPME-FSG's initial design.

#### IV. MULTI-OBJECTIVE OPTIMIZATION OF DPME-FSG

In this section, the initial design of DPME-FSG is going to be subjected to multi-objective optimization. In this regard, the multi-objective optimization procedure consists of three components: 1- ETD, 2- POCs, and 3- DMA-TOPSIS.

##### A. ETD

Selecting the DVs is the first step in multi-objective optimization. In this study, DVs represent the geometric parameters of DPME-FSG, where the width of the rotor PM, the width of the stator PM, the rotor tooth angle, and the stator tooth

TABLE 4. Orthogonal arrays.

Number of experiments	Levels of DVs			
	DV1	DV2	DV3	DV4
1	1	1	1	1
2	1	2	2	2
3	1	3	3	3
4	1	4	4	4
5	1	5	5	5
6	2	1	2	3
7	2	2	3	4
8	2	3	4	5
9	2	4	5	1
10	2	5	1	2
11	3	1	3	5
12	3	2	4	1
13	3	3	5	2
14	3	4	1	3
15	3	5	2	4
16	4	1	4	2
17	4	2	5	3
18	4	3	1	4
19	4	4	2	5
20	4	5	3	1
21	5	1	5	4
22	5	2	1	5
23	5	3	2	1
24	5	4	3	2
25	5	5	4	3

TABLE 5. Influence proportion of each DV on the OFs.

OFs	DVs			
	DV1	DV2	DV3	DV4
No-load phase voltage	29.6%	2.24%	61.04%	7.12%
Cogging torque	6.47%	18.96%	1.67%	72.9%
THD%	5.55%	8.52%	13.85%	72.08%

angle have been selected as DV1, DV2, DV3, and DV4, respectively. In this regard, Table 2 lists the DVs presented in this paper. In the Taguchi method, each DV can have a number of levels; in this work, five levels are going to be considered for each DV, as shown in Table 3. Moreover, the no-load phase voltage, cogging torque, and THD% of the no-load phase voltage are the OFs. Achieving the highest value of the no-load phase voltage as well as obtaining the lowest value in the cogging torque and THD% (for no-load phase voltage) are the goals of multi-objective optimization. Therefore, the



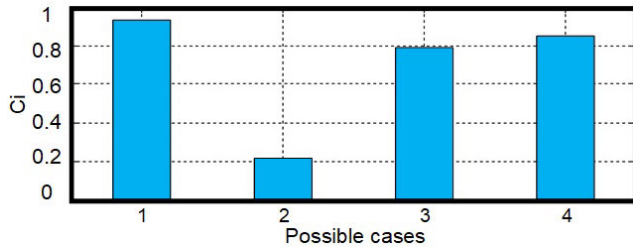


FIGURE 7. Relative closeness of each POC to the ideal solution.

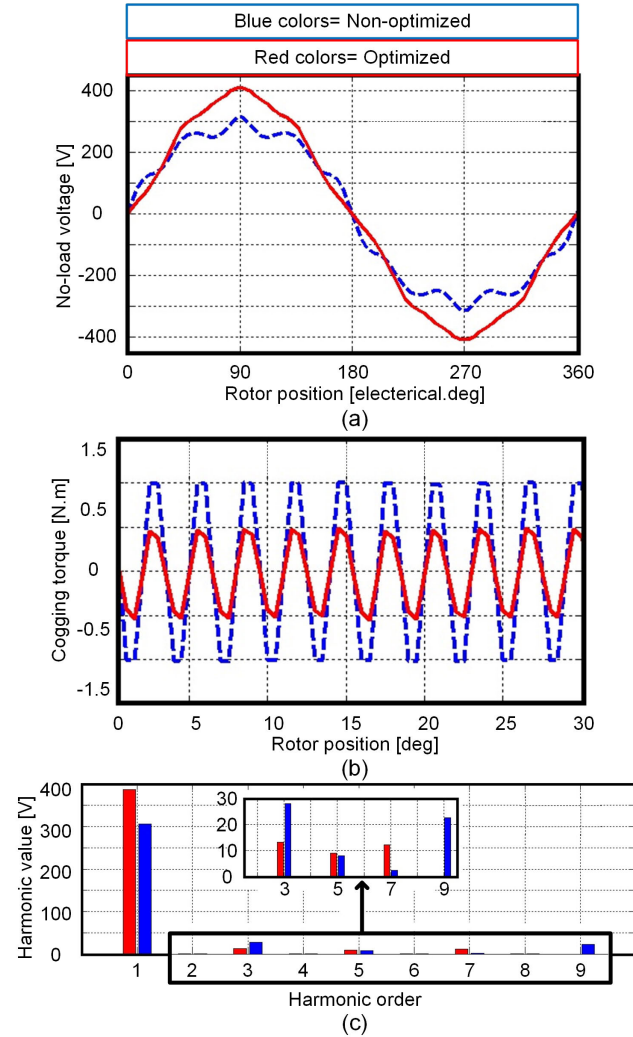


FIGURE 8. (a) No-load phase voltage, (b) cogging torque, and (c) harmonic spectrum of the initial design and optimized DPME-FSG.

ETD has been provided to evaluate the impact of each DV on the optimization objectives. In the case of four DVs with five levels,  $5^4 = 625$  experiments need to be conducted; this makes the optimization process extremely time-consuming. In order to tackle this problem, the Taguchi method provides  $L_{25}$  orthogonal arrays that reduce 625 experiments to 25. These experiments, which are known as orthogonal arrays, are presented in Table 4. In addition, the average of OFs in

TABLE 6. POCs to achieve optimum value of each OF.

OFs	DVs			
	DV1	DV2	DV3	DV4
No-load phase voltage	5	1	5	4
Cogging torque	2	4	5	2
THD%	5	5	4	1

TABLE 7. POCs of DVs.

Case	DVs				OFs		
	DV 1	DV 2	DV 3	DV 4	No-load voltage (V)	Cogging torque (N.m.)	THD %
1	5	4	5	1	402.84	0.45	4.78
2	5	5	5	1	396.43	0.97	4.07
3	5	4	5	2	384.70	0.31	7.61
4	5	5	5	2	380.35	0.34	6.75

TABLE 8. Characteristics of initial design and optimized DPME-FSG.

Designed generator	No-load phase voltage (V)	Cogging torque (N.m.)	THD%
Initial design	314.23	1	10.99
Optimized DPME-FSG	402.84	0.45	4.78

the proposed levels of each DV can be determined using MA, as addressed in (19) [21] and [22].

$$f_{mxi} = \frac{1}{n_L} \sum_{j=1}^5 f_{xi}(j) \quad (19)$$

where  $x$  is the DV,  $f_{mxi}$  is the average of the OF in the  $i$ th level of  $x$ ,  $j$  is the experiments in which  $x$  is in the  $i$ th level, and  $n_L$  is the number of levels of DVs. Figs. 6 (a) to (c) show the MA of the no-load phase voltage, cogging torque, and THD% of the no-load phase voltage, respectively. Additionally, the following equations can be used to calculate the influence proportion of each DV on the OFs ( $I_x$ ) [21], [22]:

$$f_m = \sum_{n=1}^{25} f(n) \quad (20)$$

$$v_x = \sum_{i=1}^5 (f_{mxi} - f_m)^2 \quad (21)$$

$$I_x = \frac{v_x}{\sum_{s=1}^4 v_s} \quad (22)$$

where  $f_m$  is the overall mean of the OF,  $f(n)$  is the OF,  $n$  is the number of experiments,  $v_x$  is the variance of DV  $x$  for an OF,



and  $S$  is the number of DVs. Moreover, Table 5 provides the influence proportion of each DV on the OFs.

### B. POCs

Table 6 provides the best possible combinations of each DV to achieve the optimum value of each OF. In this study, multi-objective optimization is investigated, and since there is a conflict among the best possible levels of DVs, Table 7 proposes the possible optimum cases.

### C. DMA-TOPSIS

DMA-TOPSIS is employed to determine the optimum case among POCs of DVs, as proposed in Table 7. In this regard, the DM can be expressed as:

$$DM = \begin{bmatrix} 402.84 & 0.45 & 4.78 \\ 396.43 & 0.97 & 4.07 \\ 384.70 & 0.31 & 7.61 \\ 380.35 & 0.34 & 6.75 \end{bmatrix} \quad (23)$$

In the presented DM, the first, second, and third columns refer to no-load phase voltage, cogging torque, and THD% (no-load), while the first, second, third, and fourth rows belong to each POC. Moreover, the equations given in (24) to (26) can be employed to determine the WD matrix ( $WD_{ij}$ ), where  $R_{ij}$  is the normalized decision matrix,  $X_{ij}$  is the elements of DM,  $m$  is the number of the cases,  $w_{j1}$  is the weight of the first OF, i.e., the no-load phase voltage,  $w_{j2}$  is the weight of the second OF, i.e., the cogging torque, and  $w_{j3}$  is the weight of the third OF, i.e., the THD% (for no-load phase voltage) [23], [24].

$$R_{ij} = \frac{X_{ij}}{\sum_{i=1}^m X_{ij}} \quad (24)$$

$$w_j = [w_{j1}, w_{j2}, w_{j3}] \quad (25)$$

$$WD_{ij} = R_{ij}w_j \quad (26)$$

In this study, the weights of all OFs are assumed to be equal to 1/3, considering their same importance. Moreover, the SDs can be obtained by employing the equations that are depicted in (27) and (28), where  $SD_i^+$  is the SD of the  $i$ th POC from the PIS,  $SD_i^-$  is the SD of the  $i$ th POC from the NIS,  $WD_j^+$  is the PIS in the  $j$ th column of the WD,  $WD_j^-$  is the NIS in the  $j$ th column of the WD, and  $n_o$  is the number of POCs [25].

$$SD_i^+ = \sqrt{\sum_{j=1}^{n_o} (WD_j^+ - WD_{ij})^2} \quad (27)$$

$$SD_i^- = \sqrt{\sum_{j=1}^{n_o} (WD_j^- - WD_{ij})^2} \quad (28)$$

The relation of  $C_i$  can be expressed as (29), as well as the case with the highest value of  $C_i$  is the best combination.

$$C_i = \frac{SD_i^-}{SD_i^- + SD_i^+} \quad (29)$$

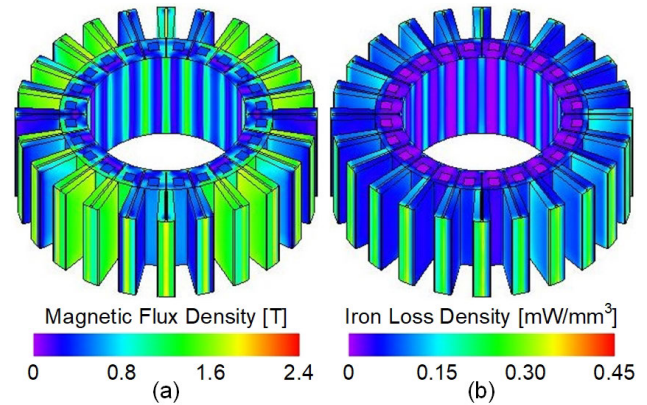


FIGURE 9. (a) Magnetic flux density and (b) iron loss density in the stator core of the DPME-FSG.

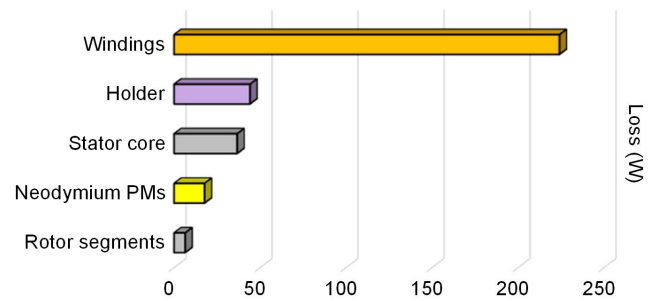


FIGURE 10. Losses in various parts of the DPME-FSG (calculated by 3-D FEM).

In this regard, Fig. 7 shows the  $C_i$  of the four possible cases, indicating that the highest value of  $C_i$  is associated with the first case, which is selected as the optimum combination of DVs. Moreover, Fig. 8 compares the output characteristics of the initial design and the optimized DPME-FSG. In the initial design and the optimized DPME-FSG, the peak value of the no-load phase voltage is  $\sim 314$  V and  $\sim 403$  V, respectively (see Fig. 8 (a)). Also, the peak value of the cogging torque, which in the initial design was 1 N.m., was reduced to 0.45 N.m. in the optimized machine (see Fig. 8 (b)), while the THD% of the no-load phase voltage was 10.99% in the initial design, but after optimization, it decreased to 4.78% (see Fig. 8 (c)). In this context, the output characteristics of the initial design and the optimized DPME-FSG are listed in Table 8. The comparison between the initial and final designs of the DPME-FSG demonstrates considerable improvements in achieving the aims of multi-objective optimization, namely in maximizing the no-load phase voltage, minimizing cogging torque, and reducing THD%.

### V. PERFORMANE EVALUATION OF DPME-FSG

In this section, the proposed DPME-FSG is going to be evaluated from the viewpoints of electromagnetic, thermal, and PMs' demagnetization, and it is also compared to its basic topology from the aspects of electromagnetic and thermal,



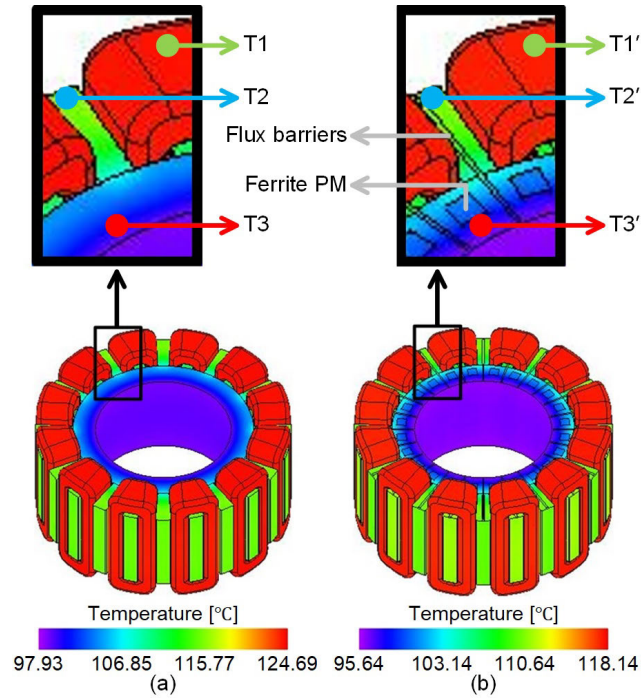


**FIGURE 11.** (a) Temperature distribution in the stationary parts of the basic topology and (b) temperature distribution in the stationary parts of the DPME-FSG.

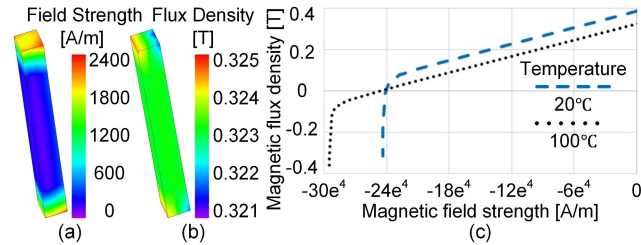


**FIGURE 12.** (a) Magnetic field strength, (b) magnetic flux density, and (c) B-H curve for ferrite PM.

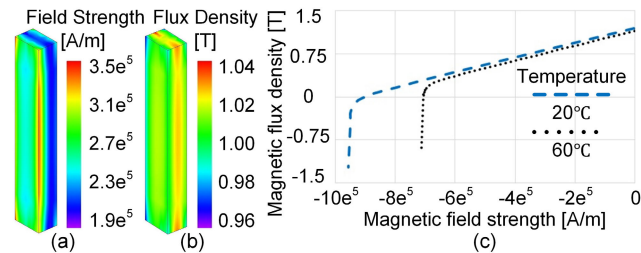


**FIGURE 13.** (a) Magnetic field strength, (b) magnetic flux density, and (c) B-H curve for neodymium PM.

which is distinguished from DPME-FSG due to the lack of stator PMs and barriers.

#### A. IN TERMS OF ELECTROMAGNETIC ANALYSIS

Adding ferrite PMs to the stator yoke of the DPME-FSG will increase its power density compared to its basic topology. Also, the peak of the no-load phase voltage and THD%

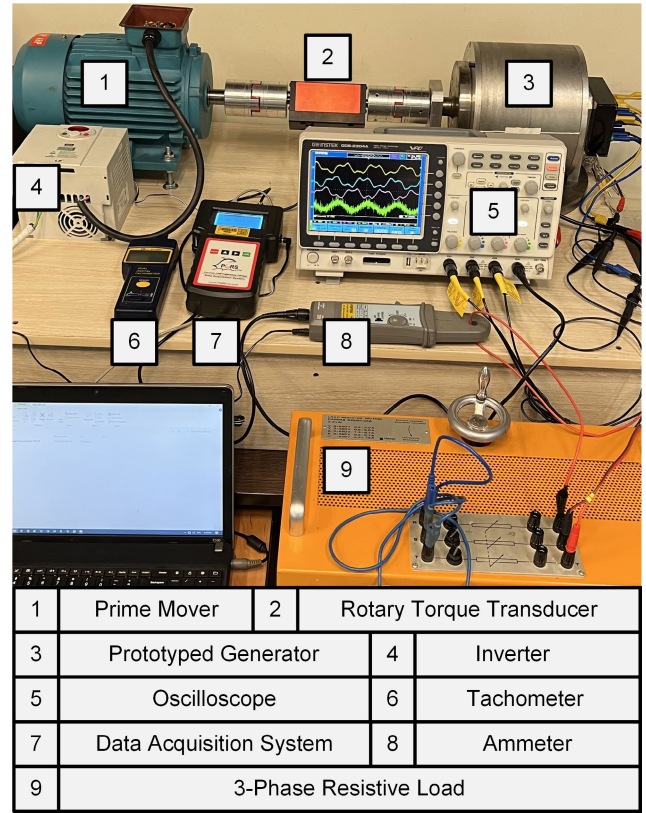


**FIGURE 14.** Test rig for the validation of DPME-FSG.

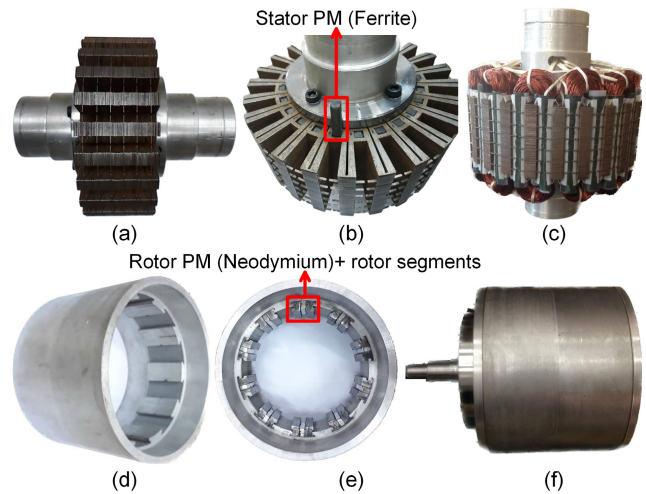


**FIGURE 15.** Various parts of the prototyped machine: (a) stator core and stationary shaft; (b) stator and ferrite PMs; (c) stationary parts; (d) holder; (e) rotating parts; and (f) assembled DPME-FSG.

(no-load) for the DPME-FSG are  $\sim 403\text{V}$  and  $\sim 4.8\%$ , whereas they are  $\sim 398\text{V}$  and  $\sim 6.4\%$  for the basic topology; however, the cogging torque of the basic topology is slightly lower than that of the DPME-FSG. Furthermore, the magnetic flux density in the stator core of the DPME-FSG is shown in Fig. 9 (a), and it can be seen that the magnetic flux density distribution in the stator core is rational. The iron loss density



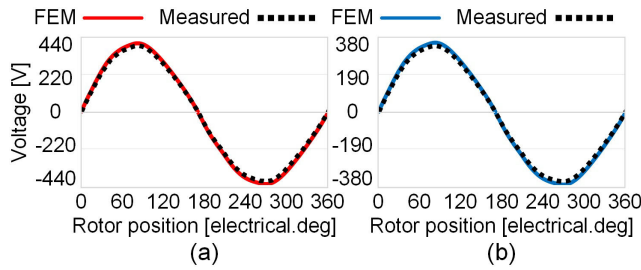


FIGURE 16. (a) No-load phase voltage and (b) full-load phase voltage.

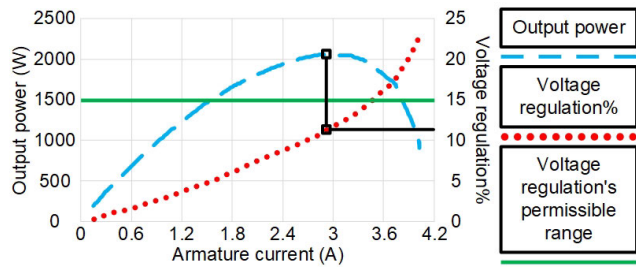


FIGURE 17. Loading curve of the prototyped DPME-FSG.

in the stator core is shown in Fig. 9 (b). It is evident that the stator teeth, which are located in front of the air-gap, exhibit the highest value of the loss density. Fig. 10 also presents the loss values for each part of the DPME-FSG. This figure clearly shows that the windings with the value of 224 W exhibit the highest losses, while the rotor segments with the value of 6.4 W have the lowest losses.

### B. IN TERMS OF THERMAL ANALYSIS

The presence of barriers in the stator teeth of the DPME-FSG serves two purposes: it separates the positive and negative half cycles of the flux linkage between the rotor segments and stator teeth, and it has a favorable effect on the temperature of various parts of the DPME-FSG. Fig. 11 shows the temperature distribution in the stationary parts of the basic topology and DPME-FSG. T1 and T1' indicate two analogous points measured at the end-winding of the basic topology and DPME-FSG, respectively. The temperature values at these points are 124.12°C and 117.59°C, respectively. T2 and T2' are two identical points measured at the stator tooth of the basic topology and DPME-FSG, respectively, with temperatures of 118.82° and 111.73°. Additionally, T3 and T3' represent two similar points measured at the stator yoke of the basic topology and DPME-FSG, respectively, with temperatures of 100.89°C and 98.71°C. By comparing the temperature values of the basic topology and DPME-FSG, the temperature drop in DPME-FSG can be observed.

### C. IN TERMS OF DEMAGNETIZATION ANALYSIS

In the DPME-FSG, which employs two types of PMs, demagnetization analysis of the PMs is inevitable, as demagnetization of the PMs leads to a drop in the machine's

TABLE 9. Torque measurements under conditions of no-load and full-load.

Torque	3-D FEM (N.M.)	Measured (N.M.)	Error%
Cogging torque (peak)	0.45	0.49	8.88
Rated torque (RMS)	33.61	30.95	7.91

performance. In this regard, Figs. 12 and 13 show the magnetic field strength distribution, magnetic flux density distribution, and B-H curve for the AC-8 ferrite PM and N35 neodymium PM, respectively. Due to the fact that the temperature value of the stator PM and rotor PM for the DPME-FSG is 101°C and 59°C, respectively, the B-H curve related to temperatures of 20°C (reference temperature) and 100 °C for the stator PM as well as the B-H curve related temperatures of 20°C and 60 °C for the rotor PM are extracted from the data sheets of the Arnold factory. In this regard, the values of the magnetic field strength and magnetic flux density for the ferrite PMs and the neodymium PMs that are presented in Figs. 12 and 13 demonstrate that the stator PMs and the rotor PMs do not demagnetize.

## VI. EXPERIMENTAL VERIFICATIONS

As shown in Fig. 14, an experimental platform has been developed to verify the results of the 3-D FEM-analyzed optimization objectives, including no-load phase voltage, cogging torque, and THD% (no-load). To carry out an in-depth assessment, the prototyped DPME-FSG is also evaluated under full-load. Fig. 15 shows the various parts of the prototyped DPME-FSG. As shown in this figure, the silicon steel M600 laminated stator core with AC-8 ferrite PMs is affixed to the structural steel 316 stationary shaft, while windings are wound as 3-phase on stator teeth. Moreover, silicon steel M600 laminated rotor segments with N35 neodymium PMs are affixed to the aluminum holder, followed by the addition of caps, pillar, and the rotating shaft. Fig. 16 (a) shows the no-load phase voltage of the optimized DPME-FSG. As shown in this figure, the peak value of the back-EMF measured in the lab is 387.1 V, which is ~3.89% less than its predicted value by the FEM. Moreover, the rated phase voltage of the optimized DPME-FSG is shown in Fig. 16 (b), where the peak value of the full-load phase voltage measured in the lab is 334.4 V and its value in FEM is 350.9 V. Fig. 17 also depicts the curves related to the output power, current, and voltage regulation% of the optimized and prototyped DPME-FSG. As shown in this figure, the voltage regulation% should not exceed 15% regarding the system's requirements, whereas the nominal output power of the DPME-FSG in the lab is ~2.1 kW, which is within the acceptable range for voltage regulation%.



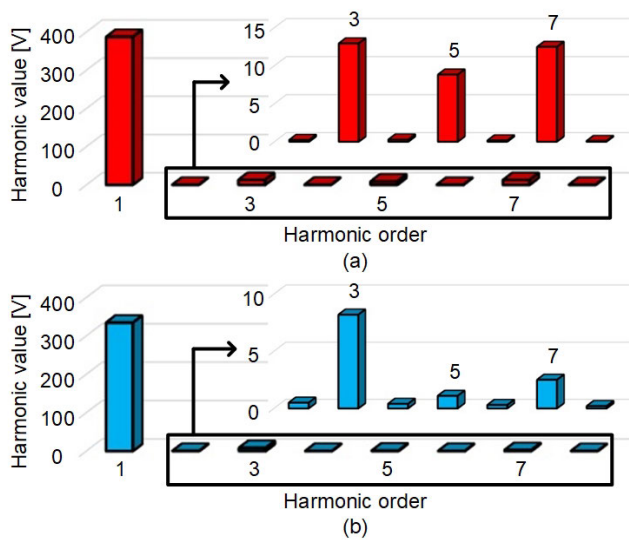


**FIGURE 18.** (a) Harmonic spectrum at no-load and (b) harmonic spectrum at full-load.

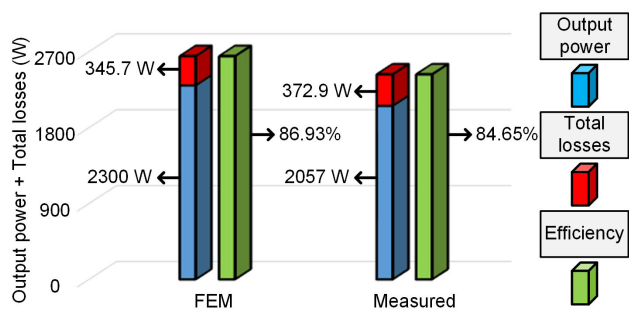


**FIGURE 19.** Evaluation of the output power and losses of the DPME-FSG.

Furthermore, Table 9 presents the values associated with the cogging torque and the rated torque. The laboratory measurements indicate that the peak value of the cogging torque is 0.49 N.m. and the RMS value of the rated torque is 30.95 N.m. However, the FEM predicts that these values are 0.45 N.m. and 33.61 N.m., respectively. On top of that, the harmonic spectrum of the DPME-FSG under both no-load and full-load conditions can be seen in Fig. 18 (in the lab). Where the THD% in the no-load condition is 4.99%, while it is 2.34% in the full-load condition. Fig. 19 compares the output power, total losses, and efficiency calculated between the 3-D FEM and lab results. As can be seen from Fig. 19, the difference between the 3-D FEM and the experimental test in terms of output power, total losses, and efficiency is 10.56%, 7.86%, and 2.28%, respectively. Moreover, Fig. 20 provides the output power and temperature values of the DPME-FSG at various operating points. As can be seen from this figure, the temperature of the machine at 200% of the rated load, calculated by the 3-D FEM, is within a prohibited temperature range. Consequently, the output power and temperature of the DPME-FSG at 200% of the rated load are not measured in the laboratory in order to avoid damage to the windings and PMs.

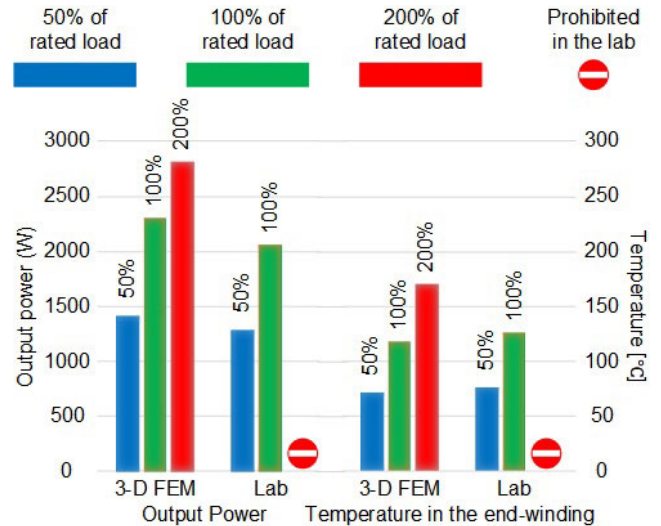


**FIGURE 20.** Evaluation of the DPME-FSG performance under various resistive loads.

## VII. CONCLUSION

In this paper, an outer rotor DPME-FSG was designed and optimized for use in DDWTs. This prototyped generator gains simultaneously from ferrite PMs inside the stator yoke and neodymium PMs between the rotor segments. The initial design of the DPME-FSG is optimized to enhance the no-load phase voltage, cogging torque, and THD% (no-load). This multi-objective optimization is carried out in three steps, i.e., ETD, POCs, and DMA-TOPSIS. The no-load phase voltage of the DPME-FSG has increased by 28.2% compared to the initial design, whereas its cogging torque and THD% have decreased by 55% and 56.5%, respectively, related to the initial design. In addition, the power density of the DPME-FSG is higher than that of the basic topology, which employed only neodymium PMs in the rotor. The results achieved in the laboratory under both no-load and full-load conditions are in excellent agreement with the 3-D FEM simulation analysis.

## ACKNOWLEDGMENT

This study was carried out within the MOST-Sustainable Mobility Center and received funding from the European Union Next-Generation EU (PIANO NAZIONALE DI RIPRESA E RESILIENZA (PNRR) – MISSIONE 4 COMPONENTE 2, INVESTIMENTO 1.4 – D.D. 1033, 17/06/2022, CN00000023). This manuscript reflects only the authors' views and opinions; neither the European Union nor the European Commission can be considered responsible for them.

## REFERENCES

- [1] C. M. Emeghara, S. M. Mahajan, and A. Arzani, "Direct power control of a surface-mounted permanent magnet synchronous generator wind turbine for offshore applications," *IEEE Access*, vol. 11, pp. 62409–62423, 2023.
- [2] A. Ghaheri, E. Afjei, and H. Torkaman, "A novel axial air-gap transverse flux switching PM generator: Design, simulation and prototyping," *IET Electr. Power Appl.*, vol. 17, no. 4, pp. 452–463, Apr. 2023.



- [3] W. Ullah, F. Khan, and S. Hussain, "Investigation of inner/outer rotor permanent magnet flux switching generator for wind turbine applications," *IEEE Access*, vol. 9, pp. 149110–149117, 2021.
- [4] S. Li, Y. Jiang, B. Fang, and C. Wang, "Characteristics analysis of inertia damping of grid-connected system of direct-drive wind power generation," *IEEE Access*, vol. 8, pp. 189802–189810, 2020.
- [5] W. Ullah, F. Khan, U. B. Akuru, S. Hussain, M. Yousuf, and S. Akbar, "A novel dual electrical and dual mechanical wound field flux switching generator for co-rotating and counter-rotating wind turbine applications," *IEEE Trans. Ind. Appl.*, vol. 60, no. 1, pp. 184–195, Jan./Feb. 2024.
- [6] F. Farrokh, A. Vahedi, H. Torkaman, M. Banejad, and V. Z. Faradonbeh, "A 2D hybrid analytical electromagnetic model of the dual-stator axial-field flux-switching permanent magnet motor," *IET's Power Appl.*, vol. 18, no. 2, pp. 252–264, Feb. 2024.
- [7] W. Ullah, F. Khan, S. Hussain, M. Yousaf, and S. Akbar, "Analytical modeling and optimization of partitioned permanent magnet consequent pole switched flux machine with flux barrier," *IEEE Access*, vol. 10, pp. 123905–123919, 2022.
- [8] X. Xu, W. Zhang, J. Cheng, J. Zhao, and F. Qian, "Design and optimization of axial field flux-switching magnetic gear composite motor based on varying-network magnetic circuit," *IEEE Access*, vol. 11, pp. 53749–53759, 2023.
- [9] G. Zhao, Z. Li, W. Hua, X. Jiang, and P. Su, "Comparative study of winding configuration on a multitooth flux-switching permanent magnet machine," *IEEE Trans. Magn.*, vol. 58, no. 2, pp. 1–5, Feb. 2022.
- [10] S. M. Saghin, A. Ghaehri, H. Shirzad, and E. Afjei, "Performance optimization of a segmented outer rotor flux switching permanent magnet motor for direct drive washing machine application," *IET Electr. Power Appl.*, vol. 15, no. 12, pp. 1574–1587, Dec. 2021.
- [11] J. Zhao, W. Fu, Y. Zheng, Z. Chen, and Y. Wang, "Comparative study of modular-stator and conventional outer-rotor flux-switching permanent-magnet motors," *IEEE Access*, vol. 7, pp. 38297–38305, 2019.
- [12] B. Ullah, F. Khan, Z. Ahmad, S. Akbar, A. H. Milyani, and A. A. Azhari, "Performance analysis of a modular E-shaped stator hybrid excited flux switching motor with flux gaps," *IEEE Access*, vol. 10, pp. 116098–116106, 2022.
- [13] Z. Chen and Y. Cui, "Numerical simulation and experimental validation of a flux switching permanent magnet memory machine," *IEEE Access*, vol. 8, pp. 194904–194911, 2020.
- [14] W. Ullah, F. Khan, E. Sulaiman, I. Sami, and J.-S. Ro, "Analytical sub-domain model for magnetic field computation in segmented permanent magnet switched flux consequent pole machine," *IEEE Access*, vol. 9, pp. 3774–3783, 2021.
- [15] W. Ullah, F. Khan, E. Sulaiman, M. Umair, N. Ullah, and B. Khan, "Analytical validation of novel consequent pole E-core stator permanent magnet flux switching machine," *IET Electr. Power Appl.*, vol. 14, no. 5, pp. 789–796, May 2020.
- [16] M. Farahzadi, K. Abbaszadeh, and S. Mirnikjoo, "Electromagnetic-thermal analysis of a hybrid-excited flux switching permanent magnet generator for wind turbine application," *IEEE Trans. Energy Convers.*, vol. 38, no. 3, pp. 1962–1973, Sep. 2023.
- [17] A. Zarghani, H. Torkaman, N. Arbab, and M. Sedigh Toulabi, "Lumped parameter thermal network for thermal analysis of a rotor-excited axial flux switching machine with electromagnetic-thermal design," *Measurement*, vol. 193, Apr. 2022, Art. no. 110971.
- [18] S. Nath, J. Wu, Y. Zhao, and W. Qiao, "Low latency bearing fault detection of direct-drive wind turbines using stator current," *IEEE Access*, vol. 8, pp. 44163–44174, 2020.
- [19] S. A. Mirnikjoo, F. Asadi, K. Abbaszadeh, and S. E. Abdollahi, "Effect of rotor topology on the performance of counter-rotating double-sided flux switching permanent magnet generator," *IEEE Trans. Energy Convers.*, vol. 37, no. 1, pp. 65–74, Mar. 2022.
- [20] F. Farrokh, A. Vahedi, H. Torkaman, and M. Banejad, "Design and comparison of dual-stator axial-field flux-switching permanent magnet motors for electric vehicle application," *IET Electr. Syst. Transp.*, vol. 13, no. 2, p. e12074, Jun. 2023.
- [21] M. Naseh, S. Hasanzadeh, S. M. Dehghan, H. Rezaei, and A. S. Al-Sumaiti, "Optimized design of rotor barriers in PM-assisted synchronous reluctance machines with Taguchi method," *IEEE Access*, vol. 10, pp. 38165–38173, 2022.
- [22] W.-C. Weng, "Design and optimization of compact microstrip wide-band bandpass filter using Taguchi's method," *IEEE Access*, vol. 10, pp. 107242–107249, 2022.
- [23] S. A. Mirnikjoo, K. Abbaszadeh, and S. E. Abdollahi, "Multiobjective design optimization of a double-sided flux switching permanent magnet generator for counter-rotating wind turbine applications," *IEEE Trans. Ind. Electron.*, vol. 68, no. 8, pp. 6640–6649, Aug. 2021.
- [24] T. Mahmood, K. Hussain, J. Ahmmad, U. U. Rehman, and M. Aslam, "A novel approach toward TOPSIS method based on lattice ordered T-bipolar soft sets and their applications," *IEEE Access*, vol. 10, pp. 69727–69740, 2022.
- [25] W. Ullah, F. Khan, and S. Hussain, "A novel dual rotor permanent magnet flux switching generator for counter rotating wind turbine applications," *IEEE Access*, vol. 10, pp. 16456–16467, 2022.



**MOHAMMAD FARAHZADI** was born in Tehran, Iran. He received the master's degree in power electronics and electric machines from the University of Science and Culture, Tehran, Iran, in 2021. He is currently an Electrical Machine Designer with the Niroo Research Institute and a Researcher with the K. N. Toosi University of Technology, Tehran. His research interests include mechanical and electromagnetic analyses by FEM (2D/3D), assessment of demagnetization of permanent magnets, thermal modeling by FEM, LPM, and CFD, as well as design, optimization, and prototyping of electric machines, especially machines of the flux switching permanent magnet, permanent magnet assisted synchronous reluctance, radial flux permanent magnet, axial flux permanent magnet, and doubly salient permanent magnet.



**SALMAN ALI** (Graduate Student Member, IEEE) received the B.S. degree in electrical engineering from Federal Urdu University, Islamabad, and the master's degree in electrical engineering from COMSATS University Islamabad. He is currently pursuing the Ph.D. degree with the University of Cassino and Southern Lazio, Italy. As a Young Researcher, he has eight publications, including a patent. He is well-versed in power electronics, renewable energy technologies, and power and energy. His research interest includes electrical engineering, with a specialization in electrical machine design. He is a Secretary of the Industrial Electronics Chapter of the IEEE Italy Section.



**SEYEDARMIN MIRNIKJOO** was born in Rasht, Iran, in February 1994. He received the M.Sc. degree (Hons.) in electrical engineering–electrical machines and power electronics from the K. N. Toosi University of Technology, Tehran, Iran, in 2020. He is currently pursuing the Ph.D. degree with the Electrical Engineering Department, Polytechnique Montréal, Montreal, QC, Canada. His research interests include electromagnetic transients and design, modeling, optimization, fault diagnosis, prototyping, and control of electrical machines.





**KARIM ABBASZADEH** (Senior Member, IEEE) received the B.S. degree in communication engineering from the Khaled Nasir Toosi University of Technology, Tehran, Iran, in 1991, and the M.S. and Ph.D. degrees in electrical engineering from the Amir Kabir University of Technology, Tehran, in 1997 and 2000, respectively. From 2001 to 2003, he was a Research Assistant with the Department of Electrical Engineering, Texas A&M University, College Station, TX, USA. He is currently a Professor with the Department of Electrical Engineering, K. N. Toosi University of Technology. He is actively involved in presenting short courses and consulting in his area of expertise in various industries. He is the author of more than 50 published journal articles. His research interests include power electronics and dc–dc and dc–ac converters, electric machinery, variable-speed drives, and propulsion applications.



**MARYAM SALEHI** was born in Semnan, Iran, in 1993. She received the B.S. degree in electrical engineering and the M.S. degree in power electronics and electrical machinery from Shahrood University of Technology, Shahrood, Iran, in 2015 and 2019, respectively. She is currently pursuing the Ph.D. degree in permanent magnet machines with The University of North Carolina at Charlotte, Charlotte, NC, USA. Her research interests include mathematical modeling, design, magnetic, thermal and structural modeling (2D/3D), optimization, and manufacturing of electric machines, especially doubly salient permanent magnet machines, flux switching, switched reluctance, transverse flux, and axial field PM synchronous for automotive and domestic applications.

...



**FABRIZIO MARIGNETTI** (Senior Member, IEEE) received the Laurea (Hons.) and Ph.D. degrees in electrical engineering from the University of Naples Federico II, in 1993 and 1998, respectively. In 1998, he joined the University of Cassino and Southern Lazio, Italy, where he is currently a Full Professor of power electronic converters, electrical machines, and drives. He is the Founder and the CEO of the spin-off company LEDA Srl. He is the author or coauthor of 300 publications in his research field and holds three patents. His research interests include the design, analysis, and digital control of electrical machines, renewable energies, and power converters. Since 2015, he has been a fellow of the National Institute of Nuclear Physics (INFN). He won five paper awards. He is the Chair of the Industrial Electronics Chapter of the IEEE Italy Section.

Open Access funding provided by ‘Università degli Studi di Cassino e del Lazio Meridionale’ within the CRUI CARE Agreement